Journal of Environmental Chemical Engineering 14 (2026) 123120

Contents lists available at ScienceDirect

Journal of Environmental Chemical Engineering

journal homepage: www.elsevier.com/locate/jece

Plasma-activated O-Nd_2WO_6/f-CNF hybrid electrode for sensitive electrochemical detection of azathioprine in environmental water samples

Kumar Gokulkumar [a], Parthasarathi Manimaran [b], Shen-Ming Chen [b,*,1], Neeraja Bose [a], Shih-Hsuan Chen [a], Kun-Mu Lee [a,c,d,e,**,1]

[a] Department of Chemical and Materials Engineering, Chang Gung University, Taoyuan 33302, Taiwan
[b] Department of Chemical Engineering and Biotechnology, National Taipei University of Technology, Taipei City, Taiwan
[c] Center for Sustainability and Energy Technologies, Chang Gung University, Taoyuan 33302, Taiwan
[d] Division of Neonatology, Department of Pediatrics, Chang Gung Memorial Hospital, Linkou, Taoyuan 33305, Taiwan
[e] College of Environment and Resources, Ming Chi University of Technology, Taipei City 24301, Taiwan

ARTICLE INFO

Keywords:
O_2 plasma-engineered Nd_2WO_6
Carbon nanofiber hybrid
Electrochemical sensing
Trace-level drug detection
Environmental water analysis

ABSTRACT

Developing highly sensitive and selective electrochemical sensors for monitoring pharmaceutical contaminants in environmental waters remains a significant challenge. Herein, a defect-engineered composite based on oxygen plasma-treated neodymium tungstate integrated with functionalized carbon nanofibers (O-Nd_2WO_6/f-CNF) is reported for the electrochemical detection of the immunosuppressive drug azathioprine (AZP). Nd_2WO_6 nanoparticles were synthesized via a hydrothermal route and subsequently modified through oxygen plasma treatment to introduce surface oxygen defects and increase electroactive sites. The incorporation of functionalized carbon nanofibers provided a conductive framework that enhanced electron transport and improved analyte adsorption at the electrode interface. The synergistic interaction between defect-rich O-Nd_2WO_6 and the highly conductive f-CNF network significantly accelerated charge transfer kinetics and amplified the electrochemical response toward AZP. The O-Nd_2WO_6/f-CNF modified glassy carbon electrode exhibited excellent sensing performance with a low detection limit of 0.066 μM, high sensitivity of 0.74 μA μM^{-1} cm^{-2}, and a wide linear detection range of 1 μM to 360 μM and 410 μM to 1420 μM. The enhanced analytical performance arises from the increased density of oxygen-related active sites generated by plasma treatment together with the efficient electron transport pathways provided by the CNF network. Furthermore, the sensor demonstrated good operational stability, repeatability, and reproducibility. Real sample analysis in hospital wastewater, river water, and tap water showed satisfactory recoveries of 96.8–102.4%, confirming the practical applicability of the proposed sensing platform for environmental monitoring of AZP residues.

1. Introduction

Azathioprine (AZP) is a purine-analog immunosuppressive drug widely prescribed for the treatment of immune-mediated disorders such as Crohn's disease, rheumatoid arthritis, ulcerative colitis, and systemic lupus erythematosus as well as for preventing organ-transplant rejection [1–3]. Owing to its strong immunomodulatory properties, AZP is also administered for several dermatological conditions, including severe eczema and pemphigus [3,4]. Despite its therapeutic importance, AZP possesses a narrow therapeutic window, and prolonged administration or excessive dosage may result in severe adverse effects [5]. Clinical investigations have reported that long-term exposure to AZP can induce bone marrow suppression [6], hepatotoxicity [7], and increased susceptibility to infections due to reduced production of erythrocytes, leukocytes, and thrombocytes [8,9]. Such hematological complications may lead to anaemia, impaired immune response, and abnormal blood coagulation, thereby posing serious risks to patient health [8,10,11]. Furthermore, extensive use of AZP in clinical treatments has resulted in its continuous discharge into environmental water systems through hospital effluents and pharmaceutical waste streams [12–14]. The

* Corresponding author.
** Corresponding author at: Department of Chemical and Materials Engineering, Chang Gung University, Taoyuan 33302, Taiwan.
E-mail addresses: smchen@ntut.edu.tw (S.-M. Chen), kmlee@mail.cgu.edu.tw (K.-M. Lee).
[1] Equal contribution.

https://doi.org/10.1016/j.jece.2026.123120
Received 23 March 2026; Received in revised form 10 May 2026; Accepted 11 May 2026
Available online 12 May 2026

persistence of AZP residues in aquatic environments raises potential ecological concerns and highlight the need for sensitive analytical methods capable of monitoring trace levels of this drug in both biological and environmental samples.

Traditional analytical methods including high-performance liquid chromatography, nuclear magnetic resonance spectroscopy, chemiluminescence analysis, and surface-enhanced Raman spectroscopy have been widely employed for AZP determination due to their high analytical accuracy [15]. However, these techniques often involve expensive instrumentation, complex sample preparation procedures, lengthy analysis times, and the requirement for highly trained personnel [16,17]. These limitations restrict their applicability for rapid, on-site, and cost-effective monitoring of pharmaceutical residues. In contrast, electrochemical sensing technologies have emerged as powerful alternatives because of their rapid response, low operational cost, high sensitivity, and compatibility with miniaturized and portable devices [18,19]. The analytical performance of electrochemical sensors is largely governed by the physicochemical characteristics of the electrode interface. Techniques such as cyclic voltammetry (CV) provide valuable insight into redox mechanisms and electron-transfer kinetics, whereas differential pulse voltammetry (DPV) enhances the faradaic signal through pulsed potential modulation, enabling highly sensitive detection of trace analytes[20–22].

One promising strategy to overcome these limitations is the integration of advanced functional nanomaterials capable of enhancing electron transfer and catalytic activity at the electrode surface. Among various oxide systems [23], rare-earth tungstate's have attracted growing attention due to their unique electronic structures and excellent chemical stability. In particular, Nd_2WO_6, represents an emerging rare-earth metal oxide with promising electrochemical characteristics [24]. The crystal structure of Nd_2WO_6 consists of interconnected WO_6 octahedral units coordinated with Nd^{3+} ions, forming a stable Nd-O-W lattice network. This structural configuration provides abundant redox-active centers and facilitates efficient electron transfer within the oxide matrix. The presence of Nd^{3+} and W^{6+} metal centers further contributes to strong catalytic activity and promotes adsorption of electroactive molecules onto the oxide surface[25]. These characteristics make Nd_2WO_6 a promising material for electrochemical applications. Nevertheless, the intrinsic conductivity of Nd_2WO_6 is relatively limited, which may hinder rapid electron transport and reduce sensing efficiency [24].

To address this limitation, surface engineering strategies can be employed to improve the electrochemical properties of the oxide. Among these approaches, oxygen plasma treatment has proven to be an effective method for modifying the surface chemistry of metal oxides without altering their bulk crystal structure [26]. Plasma treatment introduces oxygen-related defects, hydroxyl groups, and surface functional sites, which significantly enhance catalytic activity and adsorption capability. These plasma-induced defects act as additional electroactive centers, improving charge transfer kinetics during electrochemical reactions [27,28]. In addition, combining metal oxides with conductive carbon nanomaterials has been widely recognized as an efficient strategy to improve electrical conductivity and structural stability. Carbon nanofibers (CNF) possess a one-dimensional conductive network, high surface area, and excellent electron mobility, making them ideal candidates for hybrid electrochemical systems. When functionalized with oxygen-containing groups, functionalized carbon nanofibers (f-CNFs) exhibit improved dispersibility and strong interfacial interactions with metal oxide nanoparticles [29,30].The integration of plasma-modified Nd_2WO_6 with functionalized carbon nanofibers therefore creates a synergistic hybrid architecture with enhanced electrochemical properties. In this system, the defect-rich Nd_2WO_6 nanoparticles provide abundant catalytic sites for analyte adsorption, while the conductive f-CNF network acts as an efficient electron transport pathway. This oxide–carbon hybrid structure prevents nanoparticle aggregation, increases the accessible surface area, and promotes rapid electron transfer across the electrode interface. The combined effects of plasma-induced surface defects and the conductive f-CNF framework O-Nd_2WO_6/f-CNF significantly enhance electrochemical signal amplification and sensing sensitivity.

Here, we demonstrate a plasma-treated O-Nd_2WO_6/f-CNF nanocomposite-based electrochemical sensor for AZP detection. Nd_2WO_6 nanoparticles were prepared by a hydrothermal approach and then treated with oxygen plasma to induce defects on the surface and modify the electronic properties, enhancing the number of active sites. The plasma-engineered oxide was then hybridized with functionalized carbon nanofibers (f-CNF) via an ultrasonication process, creating a highly conductive composite structure. This approach facilitates the interfacial charge transfer and synergistically combines the defect-rich Nd_2WO_6 with the conductive f-CNF network, leading to enhanced electrocatalytic performance. The optimal sensor demonstrates a broad linear range (1–1545 μM), low detection limit (0.066 μM), and high sensitivity (0.74 μA μM^{-1} cm^{-2}), which are superior to those of many recently reported sensors (including updated comparisons Table 1). Significantly, besides the typical sensing performance, the developed system exhibits a high selectivity and was successfully used for AZP sensing in hospital wastewater, river water, and tap water. This work demonstrates not only the utility of plasma-induced defect engineering but also the great potential application of the constructed sensor for pharmaceutical and environmental monitoring of immunosuppressive drugs.

2. Chemicals and methods

All reagents employed in this work were of analytical grade and procured from commercial suppliers (Sigma-Aldrich). The chemicals were used as received without any additional purification. Comprehensive details regarding the list of chemicals, preparation of buffer solutions, and the instrumentation utilized in this study are provided in the Supporting Information **Sections S1 and S2.**

2.1. Synthesis of Nd_2WO_6 Nanoparticles

Nd_2WO_6 nanoparticles were synthesized through a hydrothermal approach. Initially, 0.1 M neodymium (III) nitrate hexahydrate [$Nd(NO_3)_3{\cdot}6\ H_2O$] was dissolved in 50 mL of deionized water under magnetic stirring and heated to 50 °C for 10 min to obtain a homogeneous precursor solution. Subsequently, 0.2 M sodium tungstate dihydrate ($Na_2WO_4{\cdot}2\ H_2O$) was slowly introduced into the solution under continuous stirring to facilitate the formation of a mixed metal precursor system. The pH of the resulting solution was gradually adjusted to pH ≈ 11 using 1 M NaOH, which resulted in the formation of a pale precipitate due to the interaction between neodymium and tungstate ions. The obtained suspension was then transferred into a Teflon-lined stainless-steel autoclave and subjected to hydrothermal treatment at 180 °C for 5 h to promote crystal nucleation and growth of Nd_2WO_6 nanoparticles. After completion of the hydrothermal reaction, the autoclave was allowed to cool naturally to room temperature[31]. The resulting precipitate was collected by centrifugation, followed by repeated washing with deionized water to remove residual ions and with ethanol to eliminate possible organic impurities. Finally, the purified product was dried and subsequently calcined at 600 °C for 5 h in air to obtain well-crystallized Nd_2WO_6 nanoparticles.

2.2. Plasma modification of Nd_2WO_6

To enhance the surface activity and introduce oxygen-rich functional groups, the as-synthesized Nd_2WO_6 nanoparticles were treated under an oxygen plasma at a power of **100 W**, a pressure of **0.2 mbar**, and an exposure time of **10 min**. Initially, the dried Nd_2WO_6 powder was uniformly dispersed onto a clean glass substrate to ensure maximum exposure of the particle surface to the plasma environment. The sample

Table 1
Summary of the analytical performance of previously reported electrochemical sensors for AZP determination, presented for comparison with the current work.

S. No	Electrode	Method	Linear range (μM)	LOD	Sensitivity (μA μM^{-1} cm^{-2})	Storage stability	Real samples	Ref.
1	$FeWO_4$-WO_3/GCE	DPV	0.001–135–150 –761.3	22 nM	1.093	99.07%	human urine, river lake and sewage water samples	[44]
2	$AgBiS_2$/AGr	Amperometry	0.02 –17.44	70 nM	5.7142	____	Blood and urine	[45]
3	NNO/rGO/GCE	DPV	0.4– 693	0.0035 μM	1.14	____	water samples	[46]
4	SnS_2/C/GCE	DPV	0.4– 693	0.0057 μM	0.4325	98%	Human urine and blood	[47]
5	SiOx/C-GA/SPCE	DPV	0.02–415	2.26 nM	4.26	____	Human urine and blood	[48]
6	Mo–P_{SLS}/GCE	DPV	0.05–200	3.5 nM	6.13	92%	Rat blood serum	[49]
7	Gd_2WO_6/MWCNT/GCE	DPV	0.1–993.78	3.5 nM	0.671	____	Tap, River, Human serum, and Urine	[50]
8	g-C_3N_4/Fe_3O_4/$CoWO_4$	Fluorescence	0–0.25 μmol^{-1}	0.317 nmol L^{-1}	_____	____	Human blood serum and tablets samples	[51]
9	O-Nd_2WO_6/f-CNF	DPV	1 – 360–410 – 1420	0.066 μM	0.74	91%	hospital wastewater, Tap and River water	This work

was then placed inside a plasma reactor chamber and treated using oxygen plasma under controlled conditions. During the process, high-energy oxygen species such O*, O_2^+, and O^- radicals interact with the Nd_2WO_6 surface, inducing surface activation and defect formation. The plasma treatment was carried out for a defined duration under low-pressure conditions to generate a stable oxygen plasma atmosphere. This process promotes the formation of surface oxygen vacancies, hydroxyl groups, and chemisorbed oxygen species, while preserving the bulk crystal structure of Nd_2WO_6. As a result, the plasma-modified material, denoted as O-Nd_2WO_6, exhibits increased surface defects and oxygen-containing functional groups, which significantly improve surface reactivity and electron-transfer capability.

2.3. Preparation of functionalized carbon nanofibers (f-CNF)

To improve the dispersibility and surface reactivity of carbon nanofibers, acid functionalization was performed to introduce oxygen-containing functional groups onto the CNF surface. In brief, pristine CNFs were treated with a mixed acid solution of concentrated nitric acid and sulfuric acid (HNO_3:H_2SO_4, 1:3 v/v) under continuous stirring at 60 °C for 2 h. This oxidative treatment introduces various oxygenated functional groups such as carboxyl (–COOH), hydroxyl (–OH), and carbonyl (C═O) groups onto the CNF surface, thereby enhancing hydrophilicity, dispersion stability, and electrochemical activity. After the reaction, the acid-treated CNFs were repeatedly washed with deionized water until neutral pH was reached to remove residual acids and impurities. The resulting functionalized carbon nanofibers (f-CNF) were then dried at room temperature and stored for further composite preparation. It should be noted that the f-CNF used in this work was synthesized following our previously reported procedure [32], and only a brief description is provided here for completeness.

2.4. Preparation of O-Nd_2WO_6/f-CNF composite

The O–Nd_2WO_6/f-CNF composite was prepared using a simple ultrasonication-assisted mixing method. In brief, O–Nd_2WO_6 nanoparticles and functionalized carbon nanofibers (f-CNF) were mixed in a 1:1 mass ratio and dispersed in 40 mL of deionized water. The suspension was ultrasonicated for 45 min to achieve uniform dispersion and promote effective interaction between the oxide particles and the CNF

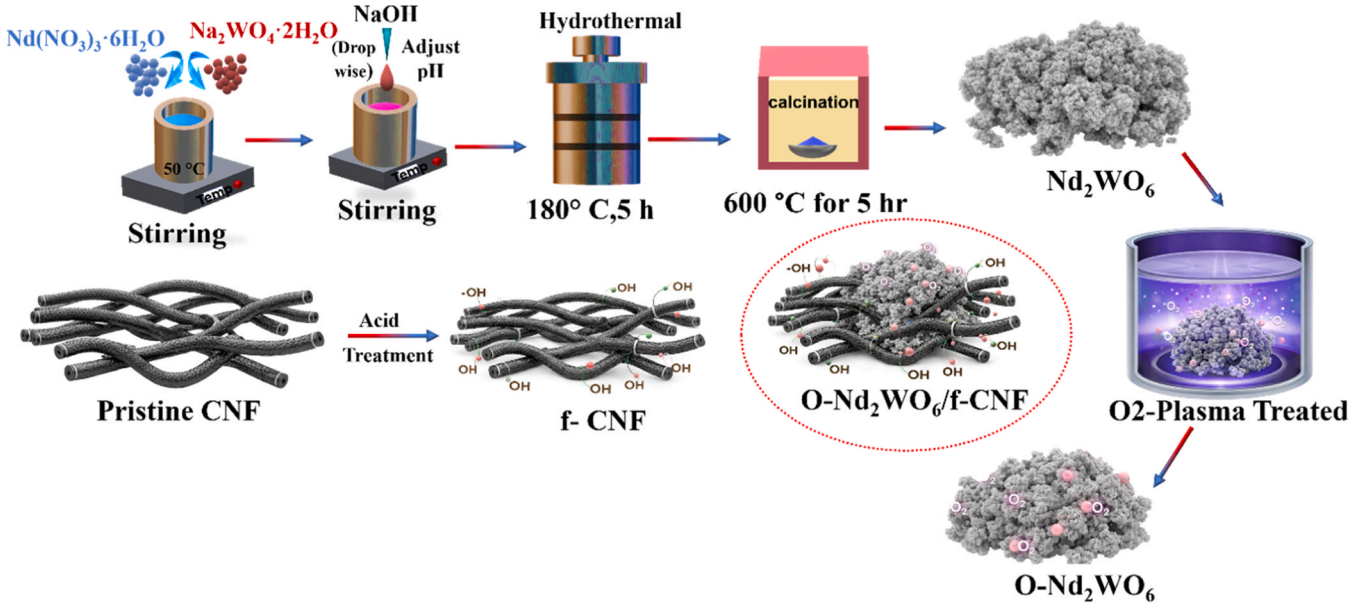

Scheme 1. Schematic illustration of the synthesis of O-Nd_2WO_6/f-CNF, including hydrothermal preparation of Nd_2WO_6, plasma treatment, CNF functionalization, and composite formation.

network. Subsequently, the mixture was magnetically stirred for 3 h to enhance interfacial coupling. The resulting composite was then collected by centrifugation, washed with deionized water and ethanol, and dried at 50–60 °C to obtain the final O–Nd_2WO_6/f-CNF hybrid material for further electrochemical studies. The overall synthesis and interfacial assembly steps are summarized schematically in Scheme 1.

2.5. Electrode fabrication

To prepare the catalyst ink, 6 mg of the O-Nd_2WO_6/f-CNF= 1:1 (w/w) composite was dispersed in 3 mL of deionized water and ultrasonicated at 200 W for 30 min to obtain a homogeneous and stable suspension. Prior to modification, the glassy carbon electrode (GCE, 3 mm diameter) was polished using 0.05 μM alumina slurry, thoroughly rinsed with deionized water, and dried to ensure a clean and active surface. Subsequently, 6 μL of the prepared ink was drop-cast onto the polished GCE surface and dried at 60 °C, forming a uniform and well-adhered film. The fabricated electrode, denoted as O-Nd_2WO_6/f-CNF/GCE, was then used for all electrochemical measurements [33].

3. Results and discussions

3.1. XRD analysis

The crystal structure and phase purity of the synthesized materials were investigated by X-ray diffraction (XRD), and the corresponding diffraction patterns are presented in Fig. 1**A**. The XRD pattern of pristine O-Nd_2WO_6 exhibits a series of well-defined diffraction peaks, indicating the formation of a crystalline oxide phase. The dominant reflections observed at approximately 27.7°, 28.4°, 29.2°, 31.4°, and 33.9° can be indexed to the characteristic crystallographic planes of monoclinic O-Nd_2WO_6, which are in good agreement with the standard reference pattern (PDF No. 00–023–1267) [34]. These diffraction peaks correspond to the ordered arrangement of $Nd^{3+}$and W^{6+} ions within the tungstate lattice framework, confirming the successful formation of the O-Nd_2WO_6 phase without the presence of secondary oxide impurities.

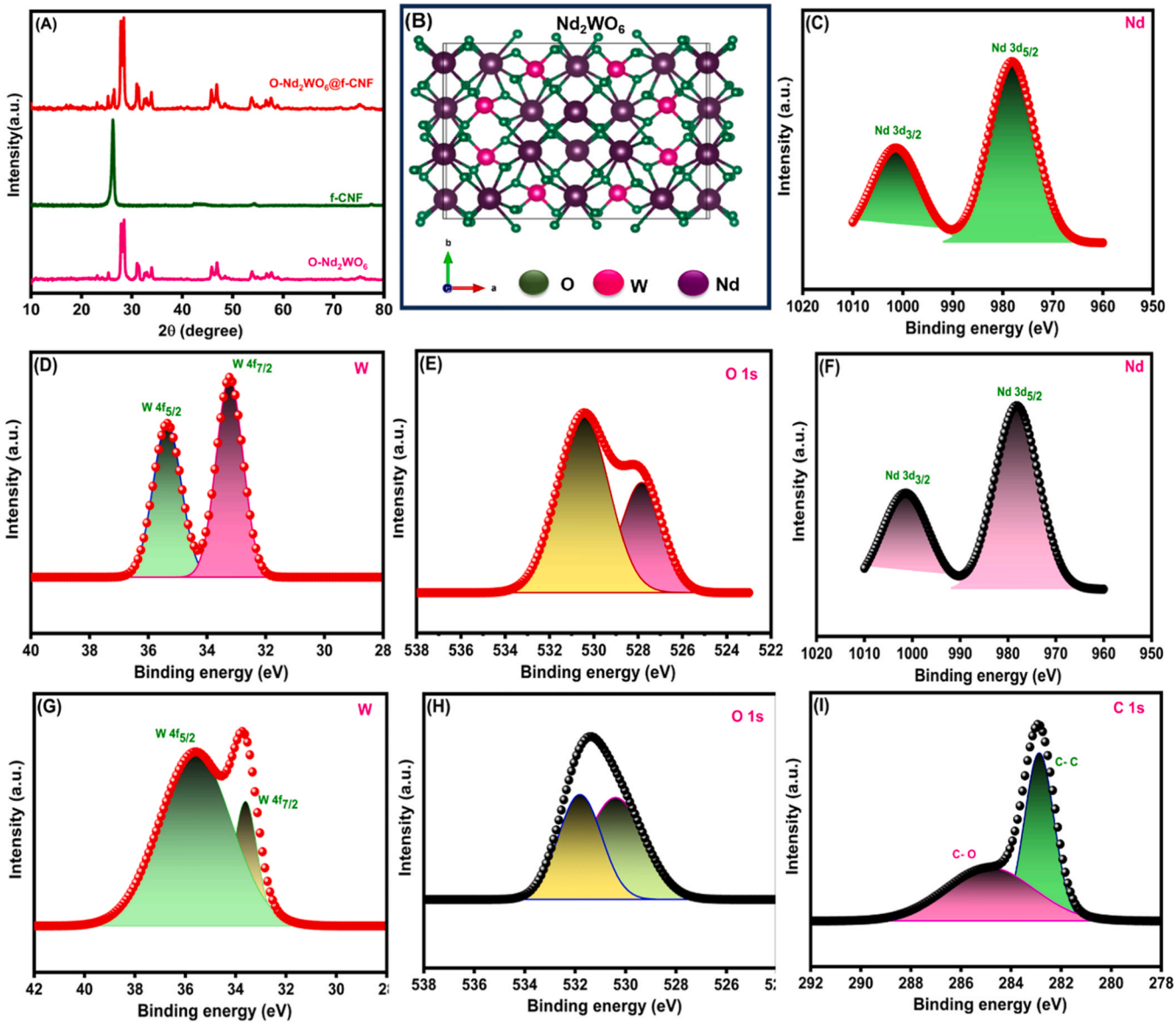

Fig. 1. Structural and surface characterization of the synthesized materials. (A) XRD patterns of O-Nd_2WO_6, f-CNF, and O-Nd_2WO_6/f-CNF confirming phase purity and successful composite formation. (B) Crystal structure representation of Nd_2WO_6. High-resolution XPS spectra of (C) Nd 3d, (D) W 4 f, and (E) O 1 s for pristine Nd_2WO_6, indicating characteristic oxidation states. XPS spectra of plasma-treated O-Nd_2WO_6/f-CNF composite showing (F) Nd 3d, (G) W 4 f, (H) O 1 s, and (I) C 1 s, confirming the presence of Nd, W, O, and C elements and the successful incorporation of oxygen functional groups and carbon nanofiber network.

The XRD pattern of f-CNF shows a broad diffraction peak centered around ~26°, which is characteristic of the (002) plane of graphitic carbon. The broad nature of this peak suggests a partially graphitized carbon structure with a stacking arrangement typical of carbon nanofibers. This graphitic feature indicates the presence of a conductive carbon framework capable of facilitating efficient electron transport.

For the O-Nd_2WO_6 /f-CNF composite, the diffraction pattern retains the characteristic peaks of Nd_2WO_6, indicating that the crystalline structure of the oxide phase remains preserved after hybridization with the carbon nanofiber matrix. The absence of additional diffraction peaks confirms that no impurity phases are formed during the composite preparation. Meanwhile, the graphitic peak associated with the CNF framework becomes less pronounced due to the dominant scattering from the crystalline oxide particles and the relatively lower diffraction intensity of carbon. The preservation of the O-Nd_2WO_6 diffraction peaks together with the presence of the graphitic carbon signal confirms the successful integration of O-Nd_2WO_6 nanoparticles with the conductive f-CNF network.

3.2. Crystallographic structure

The crystallographic structure of Nd_2WO_6 is illustrated in Fig. 1**B**, which represents the atomic arrangement within the tungstate lattice. Nd_2WO_6 adopts a monoclinic crystal structure, where tungsten atoms are coordinated by six oxygen atoms forming WO_6 octahedral units. These octahedra are interconnected through shared oxygen atoms, generating a stable three-dimensional framework. The neodymium (Nd^{3+}) ions occupy interstitial lattice positions and are coordinated with surrounding oxygen atoms, contributing to the structural stability of the oxide network. In this configuration, the oxygen atoms act as bridging ligands linking the Nd and W centers, forming a robust Nd–O–W bonding network throughout the lattice. Such a coordinated arrangement promotes efficient electron transfer pathways and structural rigidity within the Nd_2WO_6 framework. The well-defined crystal structure further supports the diffraction results observed in the XRD analysis, confirming the formation of a highly crystalline Nd_2WO_6 phase.

3.3. XPS analysis

To investigate the surface modification induced by O_2 plasma treatment, high-resolution XPS spectra were recorded for pristine and plasma-treated Nd_2WO_6, and the comparative results are shown in Fig. 1**C–H.**

The Nd 3d spectra of the pristine sample (Fig. 1**C**) display two well-defined spin–orbit doublets centered at approximately 982.4 eV (Nd $3d_{5/2}$) and 1004.8 eV (Nd $3d_{3/2}$), confirming the Nd^{3+} oxidation state [35]. After plasma treatment (Fig. 1**F**), the Nd 3d peaks remain nearly unchanged in both position and shape, indicating that the rare-earth electronic configuration is preserved. No additional components or significant shifts are observed, confirming that plasma exposure does not disturb the intrinsic Nd^{3+} lattice environment. This suggests that the modification process is confined primarily to surface oxygen coordination rather than the bulk rare-earth framework.

Clear differences are observed in the W 4 f spectra when comparing Fig. 1**D and** Fig. 1**G.** The pristine Nd_2WO_6 sample (Fig. 1**D**) exhibits sharp and symmetric W 4 $f_{7/2}$ and W 4 $f_{5/2}$ peaks characteristic of W^{6+} in the WO_6 octahedral structure [36]. After plasma treatment (Fig. 1**G**), although the dominant W^{6+} oxidation state is retained, the peak profile becomes broader and slightly asymmetric. This broadening indicates modification of the tungsten–oxygen coordination environment at the surface. Importantly, no distinct W^{5+} peak appears, confirming that the plasma does not induce bulk reduction but instead alters the electronic density and surface bonding configuration around W centers. The aligned and area-normalized comparison provided in Supplementary Fig. S1 clearly demonstrates this redistribution of spectral intensity and confirms plasma-induced surface electronic restructuring.

The most pronounced modification is observed in the O 1 s region. The pristine sample (Fig. 1**E**) shows a dominant lattice oxygen peak near 530.0 eV with a minor high-binding-energy shoulder attributed to surface hydroxyl or chemisorbed oxygen species [37]. After plasma treatment (Fig. 1**H**), the high-binding-energy component (≈531–533 eV) becomes significantly enhanced and the overall peak exhibits noticeable broadening. This increase corresponds to a higher concentration of surface hydroxyl groups, chemisorbed oxygen species, and defect-related oxygen states generated by energetic oxygen radicals during plasma exposure. The comparative aligned spectra shown in Supplementary Fig. S2 quantitatively confirm the increase in defect-associated oxygen relative to lattice oxygen, providing direct evidence of plasma-induced surface oxygen enrichment and defect formation.

Following hybridization with functionalized carbon nanofibers, the C 1 s spectrum of the composite (Fig. 1**I**) reveals a dominant C–C (sp^2) peak along with pronounced oxygen-containing carbon components such as C–O and O–C═O species [38]. The presence and enhanced intensity of these oxygenated carbon functionalities indicate strong interfacial interaction between the plasma-activated Nd_2WO_6 surface and the f-CNF network. The oxygen-enriched surface generated during plasma treatment promotes the formation of possible W-O-C or Nd-O-C interfacial linkages, facilitating electronic coupling between the oxide phase and the conductive carbon framework. This interfacial bonding is consistent with the increased oxygen-related components observed in the O 1 s spectra and confirms effective integration of Nd_2WO_6 with f-CNF.

Furthermore, the plasma-induced surface oxygen defects and oxygen-enriched active sites are closely associated with the enhanced electrochemical performance of the modified material. Compared with pristine Nd_2WO_6, the plasma-treated sample exhibited improved current response and lower charge-transfer resistance in CV and EIS analyses, respectively, indicating accelerated interfacial electron-transfer kinetics after surface activation. Although the exact quantitative defect concentration was not directly measured, the combined XPS and electrochemical results consistently suggest that oxygen plasma treatment generates surface oxygen-defect-related active sites that contribute to the improved catalytic activity of the O-Nd_2WO_6/f-CNF composite.

3.4. Surface morphology and elemental mapping analysis

The surface morphology of the synthesized materials was examined using field-emission scanning electron microscopy (FESEM), and the corresponding images are presented in Fig. 2**A–E.** The FESEM images of O-Nd_2WO_6 Figs. 2**A and** 2**B** reveal a densely aggregated nanostructured morphology composed of irregular granular particles that assemble into interconnected clusters. These oxide domains exhibit rough surfaces and porous interparticle spaces, which may facilitate electrolyte diffusion and increase the number of exposed active sites. The higher-magnification image Fig. 2**B** clearly illustrates the nanoscale texture of the oxide particles, suggesting that the plasma-assisted modification promotes the formation of surface irregularities and defect-rich domains, which are beneficial for catalytic interactions.

The morphology of functionalized carbon nanofibers (f-CNF) is displayed in Fig. 2**C.** The f-CNF sample shows a well-defined fibrous structure composed of long, interconnected carbon filaments forming a conductive network. The fibers exhibit smooth cylindrical morphology with slight surface roughness after functionalization, indicating the successful introduction of oxygen-containing surface groups that enhance interfacial interaction with metal oxide particles. The FESEM images of the O-Nd_2WO_6/f-CNF composite is shown in Fig. 2**D and E.** At lower magnification Fig. 2**D**, the composite exhibits a highly interconnected hybrid architecture in which O-Nd_2WO_6 nanoparticles are uniformly distributed throughout the fibrous CNF matrix. The oxide particles are well dispersed and anchored along the carbon nanofibers, forming an integrated oxide–carbon framework. The higher-

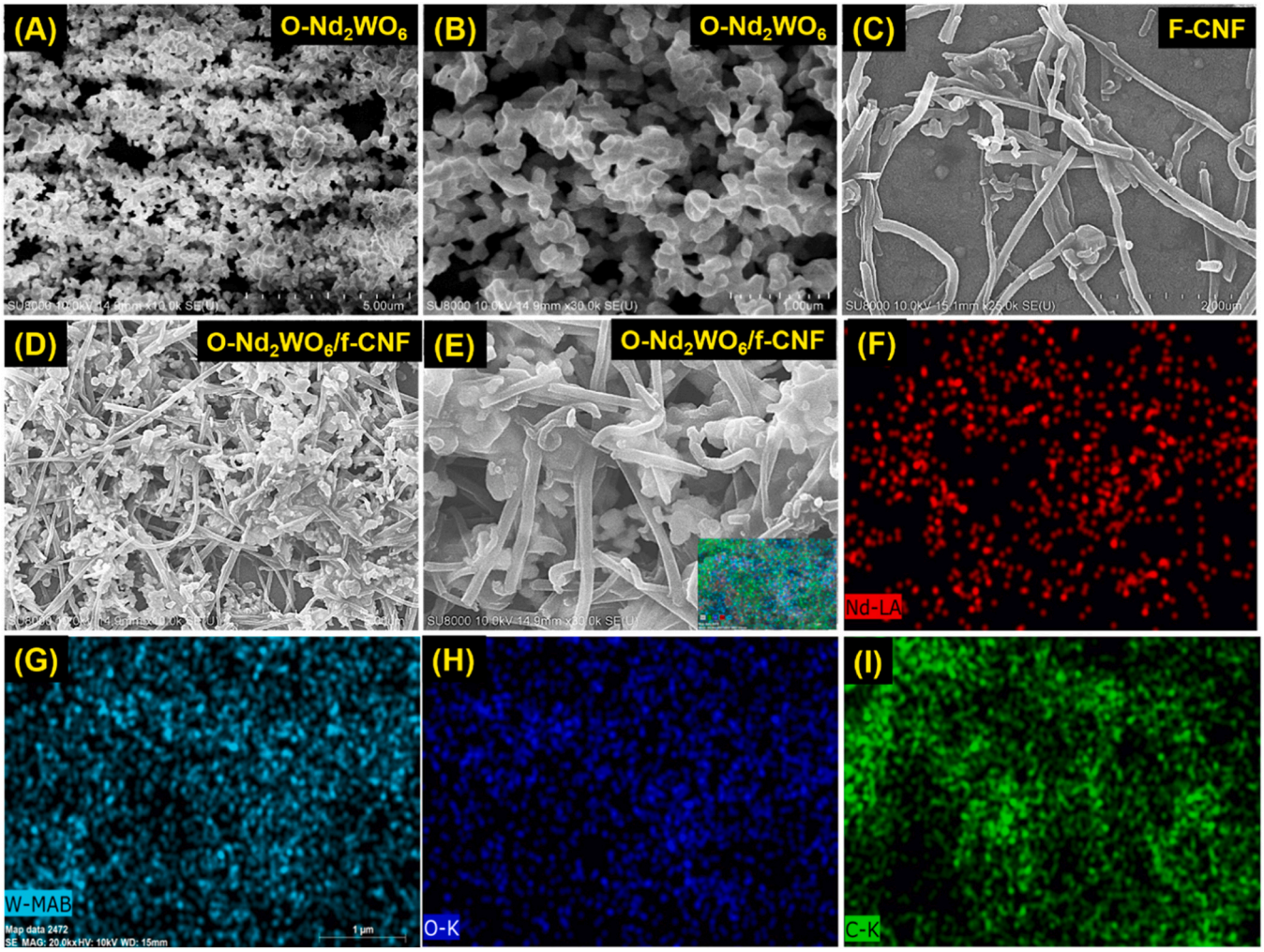

Fig. 2. FESEM images and elemental mapping analysis of the synthesized materials. (A, B) FESEM images of O-Nd_2WO_6 showing agglomerated nanostructures with rough surfaces. (C) FESEM image of f-CNF exhibiting a highly interconnected fibrous network. (D, E) FESEM images of O-Nd_2WO_6/f-CNF composite demonstrating uniform distribution and strong interaction between oxide particles and the CNF matrix. (F–I) Elemental mapping images confirming the homogeneous distribution of Nd, W, O, and C elements throughout the composite, indicating successful formation of the O-Nd_2WO_6/f-CNF hybrid structure.

magnification image Fig. 2**E** further reveals that the oxide nanoparticles are tightly attached to the CNF surface, producing intimate interfacial contact between the conductive carbon network and the oxide phase. This hybrid morphology effectively suppresses nanoparticle agglomeration while simultaneously creating continuous electron transport pathways along the CNF structure. Such structural integration is expected to enhance charge transfer efficiency and improve electrochemical performance.

3.4.1. *Elemental mapping analysis*

To further verify the elemental composition and spatial distribution of the O-Nd_2WO_6/f-CNF composite, energy-dispersive X-ray spectroscopy (EDS) elemental mapping was performed, and the results are presented in Fig. 2**F–I**. The elemental map of neodymium (Nd) in Fig. 2**F** shows a homogeneous distribution across the composite surface, confirming the uniform presence of Nd-containing oxide domains. Similarly, the tungsten (W) elemental map Fig. 2**G** demonstrates consistent dispersion of tungsten species, indicating the formation of a stable Nd_2WO_6 phase. The oxygen (O) mapping Fig. 2**H** reveals a widespread distribution throughout the observed region, corresponding to both lattice oxygen in the oxide structure and oxygen-containing surface groups generated during plasma treatment. The carbon (C) mapping shown in Fig. 2**I** confirms the continuous presence of the CNF network, which serves as a conductive scaffold supporting the oxide particles.

3.4.2. *EDX analysis*

To further confirm the elemental composition of the synthesized O-Nd_2WO_6/f-CNF composite, energy-dispersive X-ray spectroscopy (EDX) analysis was performed, and the corresponding spectrum is presented in Supplementary Fig. S3. The EDX spectrum clearly reveals the presence of Nd, W, O, and C elements, which correspond to the Nd_2WO_6 oxide phase and the carbon nanofiber matrix. The strong oxygen signal arises from both the metal–oxygen framework of Nd_2WO_6 and the oxygen-containing surface functionalities introduced during plasma treatment and CNF functionalization. Importantly, no additional impurity peaks are detected in the spectrum, confirming the high purity of the synthesized composite. The EDX results are consistent with the elemental mapping observations and further verify the successful integration of O-Nd_2WO_6 nanoparticles with the conductive f-CNF network.

3.5. *TEM analysis*

The transmission electron microscopy (TEM) images provide further insight into the internal structure and nanoscale architecture of the synthesized materials, as presented in Fig. 3**A–G**. The low-magnification TEM images of pristine O-Nd_2WO_6 Fig. 3**A–C** reveal aggregated nanocrystalline domains composed of irregularly shaped oxide particles. These particles are closely assembled into clustered structures, forming interconnected nanoscale aggregates. The contrast variations and

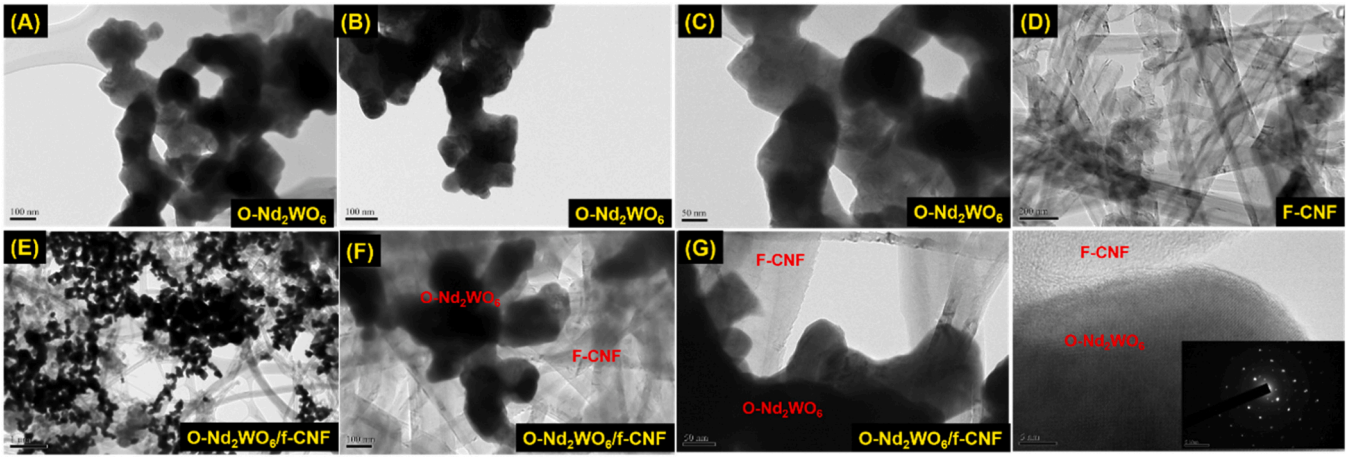

Fig. 3. TEM and HRTEM analysis of the synthesized materials. (A–C) TEM images of O-Nd_2WO_6 showing aggregated nanocrystalline structures with irregular morphology. (D) TEM image of f-CNF exhibiting a tubular and interconnected fibrous network. (E–G) TEM images of O-Nd_2WO_6/f-CNF composite demonstrating uniform anchoring of O-Nd_2WO_6 nanoparticles onto the CNF surface, suggesting enhanced interfacial contact and interaction. (H) High-resolution TEM image of the composite showing clear lattice fringes and a well-defined interface between O-Nd_2WO_6 and f-CNF; the inset SAED pattern confirms the crystalline nature of the O-Nd_2WO_6 phase.

faceted edges of the particles indicate their crystalline nature, suggesting that the oxide phase forms through nucleation and growth during the hydrothermal process. Such aggregated nanocrystalline structures expose numerous surface facets and grain boundaries, which can serve as electroactive sites for catalytic or sensing reactions. The TEM image of functionalized carbon nanofibers (f-CNF) shown in Fig. 3**D** exhibits a characteristic fibrous morphology composed of long, interconnected carbon filaments forming a conductive network. The nanofibers maintain their one-dimensional structure with smooth graphitic walls and continuous pathways along the fiber axis. This extended fibrous architecture provides an efficient electron transport network and a large interfacial area that can accommodate oxide nanoparticles.

The TEM images of the O-Nd_2WO_6/f-CNF composite Fig. 3**E–G** clearly demonstrate the formation of a hybrid oxide–carbon architecture. In the composite structure, O-Nd_2WO_6 nanoparticles are uniformly distributed and anchored along the surface of the carbon nanofibers, creating intimate contact between the oxide phase and the conductive carbon framework. The oxide particles appear to be partially wrapped and supported by the f-CNF network, which effectively suppresses nanoparticle agglomeration and improves dispersion. The high-magnification TEM image Fig. 3**G** further confirms the tight interfacial attachment between the oxide particles and the carbon nanofibers, suggesting enhanced interfacial contact within the hybrid structure. The observed interaction is mainly associated with surface-level oxygen-containing functional groups generated during oxygen plasma treatment and acid functionalization of f-CNF. Such interactions are primarily related to localized surface electronic coupling rather than the formation of a distinct crystalline interfacial layer directly visible in HRTEM analysis. Therefore, possible Nd–O–C/W–O–C linkages are inferred mainly from the combined XPS analysis, uniform nanoparticle anchoring behavior, and enhanced electrochemical performance of the composite. The inset selected area electron diffraction (SAED) pattern in Fig. 3**H** displays a series of well-defined concentric diffraction rings composed of discrete bright diffraction spots, indicating the polycrystalline nature of the O-Nd_2WO_6 nanoparticles. The observed diffraction rings correspond to the crystallographic planes of monoclinic Nd_2WO_6 which are consistent with the standard diffraction pattern of Nd_2WO_6 (PDF No. 00–023–1267). In particular, the diffraction rings can be indexed to planes associated with the dominant reflections observed in the XRD pattern, such as those corresponding to the (−321), (−411), and related crystallographic planes of Nd_2WO_6. This agreement between the SAED pattern and the XRD results confirms the formation of a well-crystallized Nd_2WO_6 phase and further verifies the structural integrity of the oxide nanoparticles within the composite architecture.

3.6. Electrochemical characterization

3.6.1. Electrochemical impedance spectroscopy (EIS) analysis

Electrochemical impedance spectroscopy (EIS) measurements were carried out in 0.1 M KCl containing 5 mM $[Fe(CN)_6]^{3-/4-}$ to evaluate the interfacial charge-transfer properties of the fabricated electrodes. The Nyquist plots Fig. 4**A** exhibit a typical semicircular region at high frequency corresponding to the charge-transfer resistance (Rct), followed by a linear region at low frequency related to diffusion-controlled processes. The bare GCE shows the largest semicircle with an Rct value of 2722 Ω, indicating sluggish electron-transfer kinetics. Upon modification with f-CNF, the Rct decreases to 2347 Ω, suggesting improved conductivity due to the carbon network. The O-Nd_2WO_6-modified electrode further reduces the Rct to 1372 Ω, attributed to the presence of redox-active Nd and W centers. Notably, the O-Nd_2WO_6/f-CNF composite exhibits the lowest Rct value of about 699 Ω, confirming enhanced electron-transfer kinetics [39]. This significant reduction arises from the synergistic effect of plasma-induced oxygen defects and the conductive CNF framework, which facilitates rapid electron transport and lowers interfacial resistance. The bar chart Fig. 4 **B** further confirms the decreasing Rct trend in the order: bare GCE > f-CNF > O-Nd_2WO_6 > O-Nd_2WO_6/f-CNF.

3.6.2. Cyclic voltammetry (CV) analysis

We evaluated the electrochemical performance of the bare/GCE, f-CNF, Nd_2WO_6, Nd_2WO_6/f-CNF and O-Nd_2WO_6/f-CNF by using CV experiments. Basically, CV experiments use a 5 mM $[Fe(CN)_6]^{4-/3-}$ redox system dissolved in 0.1 M KCl. It was performed under identical electrolyte conditions to investigate the redox behavior of the modified electrodes Fig. 4**C.** The bare GCE displays weak redox peaks with a large peak-to-peak separation ΔEp = 254 mV, indicating slow electron-transfer kinetics. The f-CNF, Nd_2WO_6 and Nd_2WO_6/f-CNF -modified electrodes show improved peak currents with reduced ΔEp values of approximately 208 mV, 209 mV and 237 mV, respectively, confirming enhanced electrochemical activity. The O-Nd_2WO_6/f-CNF electrode exhibits the highest current response with the smallest ΔEp of about 200 mV, representing a 21.3% reduction and indicating fast and quasi-reversible electron-transfer behavior. To further understand the reaction kinetics, CV measurements were conducted at different scan rates ranging from 0.02 to 0.20 V s^{-1} Fig. 4 **E.** The linear plot specifically refers to the relationship between peak current (Ip) and the square root

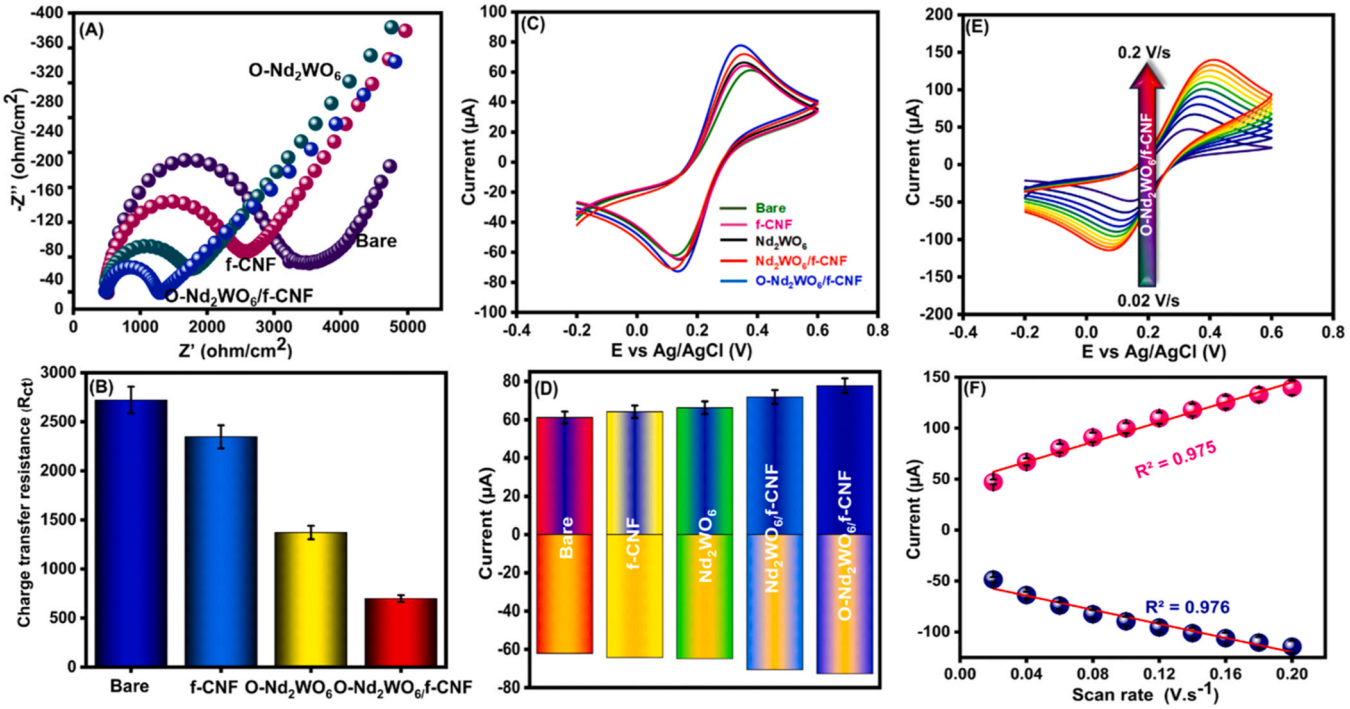

Fig. 4. (A) Nyquist plots of bare GCE, f-CNF, O-Nd_2WO_6, and O-Nd_2WO_6/f-CNF electrodes showing charge-transfer resistance behavior. (B) Corresponding Rct values comparison. (C) Cyclic voltammograms of different modified electrodes. (D) Comparison of current response for each electrode. (E) CV curves at different scan rates for O-Nd_2WO_6/f-CNF. (F) Linear relationship between peak current and scan rate, indicating diffusion-controlled kinetics.

of scan rate ($\nu^{1/2}$) derived from cyclic voltammetry, which is characteristic of a diffusion-controlled process [40]. This has now been explicitly stated, along with the corresponding linear regression equation and the correlation coefficient (y = -335.92x - 52.279, R^2 = 0.975 and y = 482.12x + 48.226, R^2 =0.9776), confirming stable and reproducible charge-transfer behavior Fig. 4**F**. The enhanced electrochemical performance of the O-Nd_2WO_6/f-CNF electrode highlights its potential for high-sensitivity sensing applications. The Randle's Sevcik equation **(**Eq. (1)**)** was also used to calculate the redox performance of the active surface area.

$$I_p = 2.69 \times 10^5 n^{\frac{3}{2}} A D^{\frac{1}{2}} C \nu^{\frac{1}{2}} \quad (1)$$

Where Ip is the redox peak current, n is the number of electrons, D is the diffusion coefficient, C is the concentration, A is the active surface area, and $V^{1/2}$ is the square root of the scan rate. Using this equation, a was calculated to be 0.076, 0.081, 0.089, 0.095 and 0.127 for bare GCE, f-CNF/GCE, Nd_2WO_6/GCE, Nd_2WO_6/f-CNF/GCE and O-Nd_2WO_6/f-CNF/GCE, demonstrating outstanding redox kinetics behaviour suitable for the electrochemical detection of APZ. The synergistic combination of expanded active surface area, reduced overpotential, and enhanced electron-transfer kinetics positions this electrode as a promising candidate for sensitive and selective APZ sensing application in environmental samples.

3.7. Electrochemical behavior and optimization studies

3.7.1. Electrochemical reaction mechanism of AZP

During electrochemical sensing, the nitro-substituted form of azathioprine (AZP–NO_2) undergoes a well-defined proton-coupled electron transfer (PCET) reduction pathway. The scan rate dependent analysis confirms a diffusion-controlled process and indicates the involvement of multiple electrons, while the pH-dependent studies reveal a linear shift in peak potential, confirming the participation of an equal number of protons and electrons. Initially, the – NO_2 group is reduced through a four-electron and four-proton transfer process, forming the intermediate hydroxylamine species (AZP–NHOH). This conversion is facilitated by the high surface activity and electron-rich catalytic sites of the O-Nd_2WO_6/f-CNF composite, which lowers the activation barrier for electron transfer. Subsequently, AZP–NHOH undergoes a reversible two-electron and two-proton redox transformation to form the nitroso derivative (AZP–NO) [41] Scheme 2 illustrates this detailed reaction pathway, showing the multi-step electrochemical behavior of AZA on the proposed sensing platform. The proposed reaction pathway was established based on the combined electrochemical observations obtained from scan-rate, pH-dependent, CV, and EIS analyses together with previously reported literature related to AZP electrochemistry and proton-coupled electron transfer mechanisms [42]. Although detailed kinetic parameters and intermediate species were not directly determined, the obtained electrochemical results strongly support the proposed reduction behavior of AZP on the O-Nd2WO6/f-CNF modified electrode.

3.7.2. Electrochemical behavior of AZP at different modified electrodes

The electrochemical response of AZP was systematically investigated using cyclic voltammetry to evaluate the catalytic contribution of each electrode modification. As shown in Fig. 5**A**, the bare glassy carbon electrode Bare GCE exhibits a relatively weak and broad cathodic peak with a current response of −5.33 μA, indicating sluggish electron transfer and limited active sites for AZP reduction. Upon modification with f-CNF, the peak current slightly increases to around −5.75 μA, which can be attributed to the excellent electrical conductivity and high surface area of the carbon nanofiber network that facilitates electron transport. Further enhancement is observed for the Nd_2WO_6-modified electrode, which shows a cathodic peak current of −6.32 μA. This improvement arises from the redox-active nature of the Nd_2WO_6 oxide, which provides additional catalytic sites and promotes efficient interaction between AZP molecules and the electrode surface. When the oxide is integrated with the conductive CNF matrix to form the O-Nd_2WO_6/f-CNF composite, the reduction current further increases to about −6.61 μA, demonstrating the synergistic coupling between the

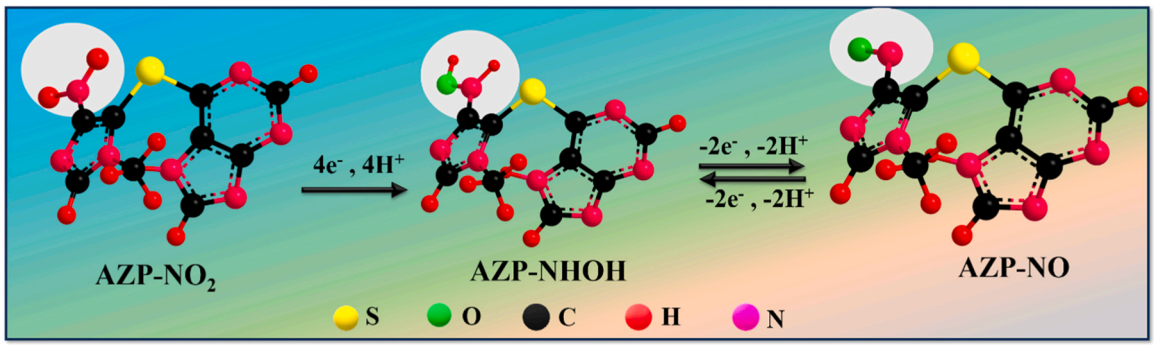

Scheme 2. Proposed electrochemical reduction mechanism of AZP showing the stepwise conversion of the –NO_2 group to –NHOH and subsequently to –NO through coupled electron proton transfer reactions.

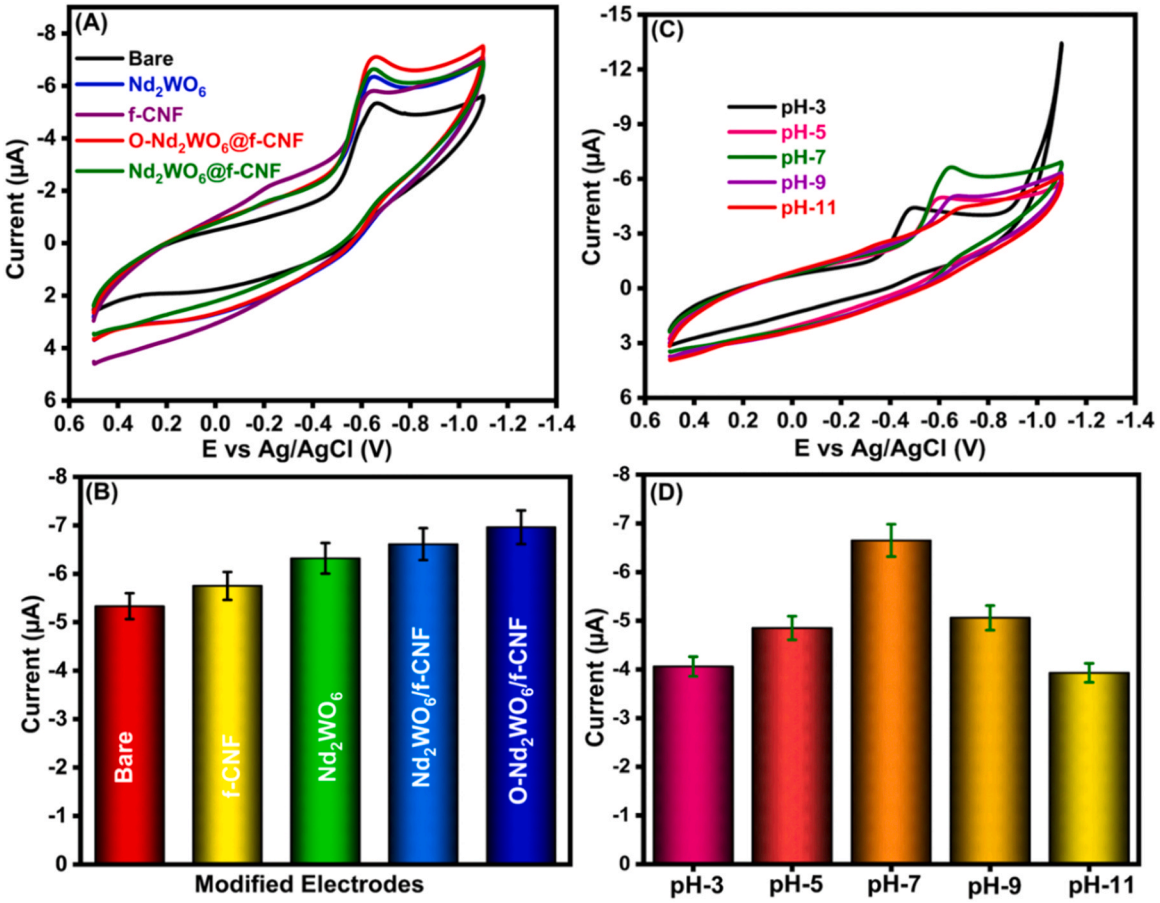

Fig. 5. Electrochemical performance of different modified electrodes toward AZP detection. (A) CV responses of bare GCE, Nd_2WO_6, f-CNF, Nd_2WO_6/f-CNF, and O-Nd_2WO_6/f-CNF modified electrodes, showing enhanced current response after composite formation. (B) Corresponding bar chart comparison of current responses for different electrodes. (C) Effect of pH (3–11) on the electrochemical response of AZP. (D) Bar chart illustrating the variation of peak current with pH, indicating optimal performance at pH 7.

oxide nanoparticles and the conductive carbon scaffold.

Notably, the oxygen-plasma-treated composite O-Nd_2WO_6/f-CNF exhibits the highest cathodic current response of -6.90 μA, confirming the superior electrocatalytic activity of the plasma-engineered hybrid electrode. The enhanced performance can be attributed to the plasma-induced surface oxygen functionalities and defect sites on Nd_2WO_6, which increase the density of electroactive sites and improve adsorption of AZP molecules. Simultaneously, the interconnected CNF network provides rapid electron transport pathways, resulting in improved charge transfer kinetics. The bar chart in Fig. 5**B** further highlights the progressive increase in peak current from the bare electrode to the plasma-treated composite, confirming the synergistic contribution of both the oxide catalyst and conductive carbon framework. Therefore, the plasma-treated Nd_2WO_6 composite was selected as the optimal sensing platform, and all subsequent electrochemical investigations were carried out using the O-Nd_2WO_6/f-CNF modified electrode.

3.7.3. Effect of solution pH on AZP electrochemical response

The influence of electrolyte pH on the electrochemical reduction of AZP was examined over and the corresponding CV responses are shown in Fig. 5**C.** The reduction peak current gradually increases from acidic conditions and reaches its maximum at pH 7, followed by a noticeable

decrease under more alkaline conditions. This trend suggests that the electrochemical reduction of AZP follows a proton-coupled electron transfer (PCET) mechanism, where proton availability plays a crucial role in the reaction kinetics. At highly acidic conditions (pH 3–5), the excess proton concentration may hinder effective adsorption of AZP onto the electrode surface, leading to relatively lower current responses. As the pH approaches neutral conditions (pH 7), the balance between proton availability and electron transfer becomes optimal, facilitating efficient reduction of AZP and enhancing the catalytic interaction between AZP molecules and the O-Nd_2WO_6/f-CNF electrode surface. This environment promotes stable hydrogen bonding and favourable electrostatic interactions, which accelerate electron transfer processes. When the pH becomes more alkaline (pH 9–11), the peak current decreases again due to reduced proton availability and partial deprotonation of AZP, which weakens adsorption and slows the electron transfer kinetics. The bar chart in Fig. 5D clearly illustrates this trend, where the maximum current response is observed at pH 7, confirming it as the optimal condition for AZP electrochemical detection using the O-Nd_2WO_6/f-CNF modified electrode.

3.8. Electrochemical response toward AZP detection

3.8.1. Effect of analyte concentration

To evaluate the quantitative sensing capability of the O-Nd_2WO_6/f-CNF modified electrode toward AZP, cyclic voltammetry measurements were performed in 0.1 M PBS (pH 7) at a fixed scan rate of 50 mV s^{-1} while gradually increasing the AZP concentration from 50 µM to 500 µM. As illustrated in Fig. 6**A**, the cathodic peak current increases progressively with increasing AZP concentration, while the peak potential remains nearly unchanged. This behavior indicates a stable and efficient electron transfer process between AZP molecules and the O-Nd_2WO_6/f-CNF electrode surface. The continuous increase in peak current demonstrates that the plasma-activated composite provides abundant electroactive sites and facilitates strong interaction between AZP and the electrode interface. The corresponding calibration plot shown in Fig. 6**B** reveals a strong linear relationship between the cathodic peak current (I_pc) and AZP concentration, yielding a correlation coefficient of $R^2 = 0.998$, confirming excellent quantitative electrochemical sensing performance. The enhanced current response can be attributed to the synergistic interaction between O-Nd_2WO_6/f-CNF network.

3.8.2. Effect of scan rate on electrochemical kinetics

The electrochemical kinetics of AZP at the O-Nd_2WO_6/f-CNF electrode were further examined by recording cyclic voltammograms at scan rates ranging from 0.02 to 0.2 V s^{-1}, as shown in Fig. 6**C**. As the scan rate increases, the cathodic peak current gradually increases while maintaining a similar voltammetric profile, indicating enhanced charge transfer and efficient electron mobility across the electrode interface. The increase in peak current with scan rate reflects the rapid electrochemical reaction of AZP at the plasma-engineered composite surface. At lower scan rates, the voltammograms display relatively well-defined

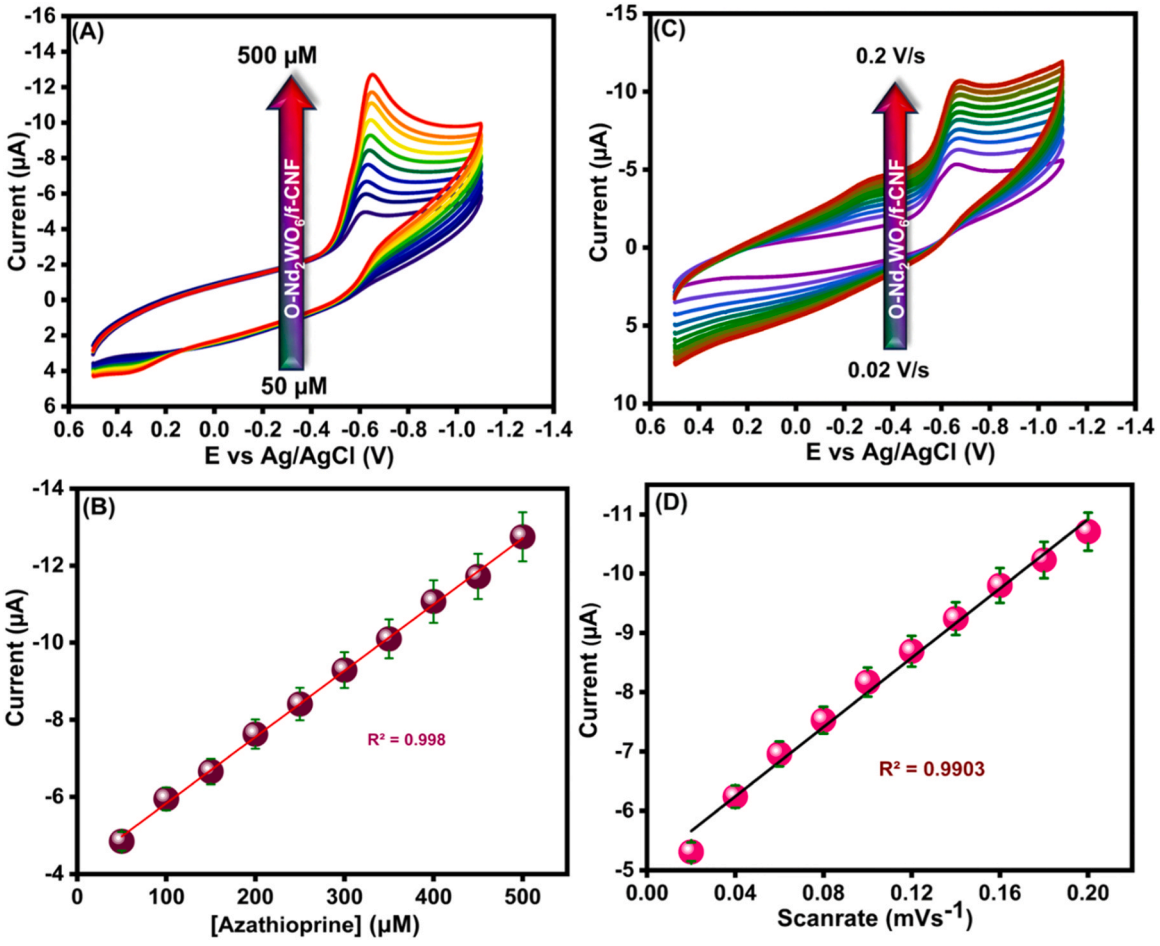

Fig. 6. Electrochemical sensing performance of the O-Nd_2WO_6/f-CNF modified electrode toward AZP detection. (A) CV responses at different AZP concentrations (50–500 µM) showing a gradual increase in peak current. (B) Corresponding calibration plot of peak current versus AZP concentration with good linearity. (C) CV responses at varying scan rates (0.02–0.2 V s^{-1}) indicating enhanced current with increasing scan rate. (D) Linear relationship between peak current and scan rate, confirming a diffusion-controlled electrochemical process.

peaks, indicating a stable diffusion-controlled electrochemical process governed by the transport of AZP molecules toward the electrode surface. With increasing scan rate, the cathodic peak shows a slight shift toward more negative potentials, suggesting the onset of a quasi-irreversible electron transfer process where interfacial kinetics begin to influence the electrochemical response.

The linear relationship between the cathodic peak current (I_{Pc}) and the square root of the scan rate shown in Fig. 6**D** $R^2 = 0.9903$ confirms that the electrochemical reduction of AZP at the O-Nd_2WO_6/f-CNF electrode is primarily diffusion-controlled. The efficient diffusion behavior can be attributed to the porous nanostructured morphology and defect-rich surface of the plasma-treated Nd_2WO_6 nanoparticles, which facilitate rapid analyte adsorption and electron transfer. Additionally, the conductive CNF network acts as an electron highway, enabling fast charge transport and improving the electrochemical kinetics of AZP reduction.

3.9. Differential pulse voltammetry sensing performance, selectivity, operational stability, and reproducibility

3.9.1. DPV determination of AZP

The quantitative detection capability of the O-Nd_2WO_6/f-CNF modified electrode toward AZP was further evaluated using differential pulse voltammetry (DPV) in 0.1 M PBS (pH 7). As illustrated in Fig. 7**A**, the cathodic peak current increases as AZP concentration rises from 1 μM to 360 μM and 410 μM to 1420 μM. Two linear ranges are present: adsorption-controlled kinetics dominate at low concentrations, while diffusion-limited processes occur at higher concentrations. This transition decreases sensitivity but demonstrates efficient electron exchange between the analyte and the plasma-engineered electrode surface. The DPV responses display well-defined peaks without noticeable broadening or potential shifting, indicating stable electrochemical behavior and fast redox kinetics. The enlarged inset in Fig. 7**A** highlights the clear response even at low concentrations, confirming the high sensitivity of the sensing interface. The corresponding calibration curve is presented in Fig. 7**B**, where the cathodic peak current exhibits a strong linear relationship with AZP concentration. Two linear regions are observed with excellent regression coefficients y = -0.0968x-3.348 ($R^2 = 0.9957$) and y = -0.0236x-15.826 ($R^2 = 0.9942$), demonstrating a wide dynamic low detection limit of 0.066 μM, high sensitivity of 0.74 μA μM^{-1} cm^{-2} of the sensor can be attributed to the synergistic coupling between plasma-activated O-Nd_2WO_6/f-CNF nanoparticles. The detection limit (LOD) of the developed sensor was calculated using the standard Eq. 2**&3**[43]

$$LOD = 3 \times \sigma / S \tag{2}$$

$$Sensitivity = \quad S/ECSA \tag{3}$$

where σ represents the standard deviation of the blank signal and s corresponds to the slope of the calibration curve.

3.9.2. Selectivity and interference study

The selectivity of the developed sensor toward AZP was examined in the presence of several potentially interfering species. As shown in Fig. 7**C**, the DPV responses were recorded in the presence of common interferents (a–f) such as a-K^+, b-Na^+, c-Fe^{3+}, D-uric acid, e-glucose, f-nitrophenol, g-cysteine, h-glutathione, i- Hg^+, while maintaining the presence of (50 μM) AZP-containing PBS (pH 7) solution at a scan rate of 50 mV^{s-1}.The electrochemical signal corresponding to AZP remained nearly unchanged, with only negligible variation in current intensity. The relative error values presented in Fig. 7**D** remain below 2–3%, confirming that the presence of these species does not significantly influence the detection signal. This excellent anti-interference performance can be attributed to the defect-rich surface of plasma-treated

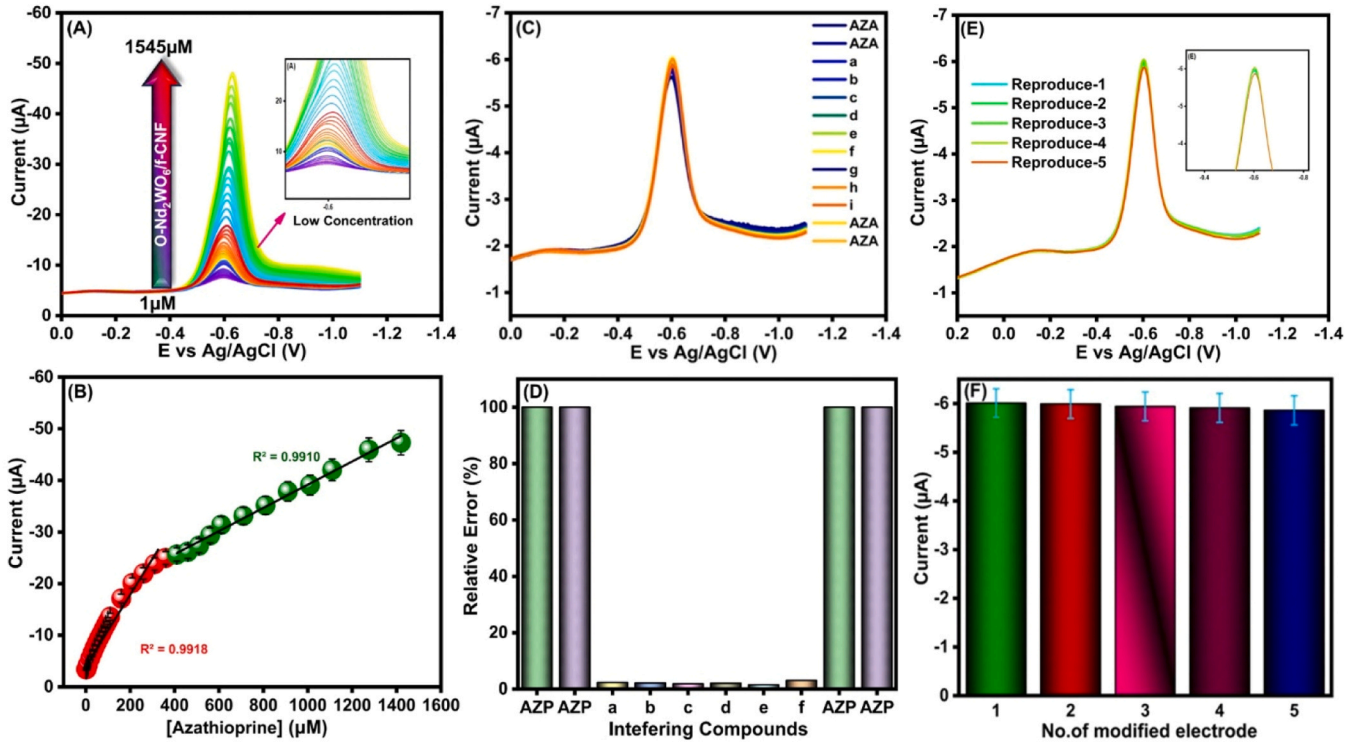

Fig. 7. Differential pulse voltammetry (DPV) performance of the O-Nd_2WO_6/f-CNF modified electrode for AZP detection. (A) DPV responses at increasing AZP concentrations (1–1545 μM), showing a gradual increase in peak current. (B) Calibration plot of peak current versus AZP concentration exhibiting two linear ranges with good correlation. (C) Selectivity study in the presence of potential interfering species, demonstrating negligible interference. (D) Corresponding relative error analysis confirming high selectivity. (E) Repeatability test showing consistent responses for multiple measurements. (F) Reproducibility study using different electrodes, indicating stable and reliable performance.

Nd_2WO_6 and the π–π interactions between AZP molecules and the conductive CNF framework, which selectively promote adsorption of the target analyte. Additionally, the oxygen-functionalized surface generated by plasma treatment enhances hydrogen-bond interactions between AZP and the electrode interface, further improving the selectivity of the sensing platform.

3.9.3. Reproducibility and stability

The reproducibility of the O-Nd_2WO_6/f-CNF modified electrode was evaluated using five independently prepared electrodes under identical experimental conditions. As shown in Fig. 7**E**, the DPV responses of the five electrodes exhibit nearly identical peak currents and overlapping voltammetric profiles, indicating excellent fabrication consistency and stable electrochemical performance, as observed in a PBS (pH 7) solution containing 50 μM AZP at a scan rate of 50 mV^{s-1}. The corresponding bar chart in Fig. 7**F** summarizes the current responses obtained from the five electrodes, showing only minor variation in peak current values. The relative standard deviation (RSD) 0.22% is found to be very low, demonstrating the high reproducibility and reliability of the electrode preparation method. Fig. S4 As can be seen from the voltametric profiles, the reduction peak observed in a PBS (pH 7) solution containing (50 μM) AZP at −0.6 V (vs. Ag/AgCl) remained remarkably stable. The reproducibility demonstrated five superior successive repeated measurements with 5% RSD value, in the presence of APZ detection. Furthermore, the reliability of the O-Nd_2WO_6/f-CNF electrode was analysed. The storage stability was assessed for 15 days. Table 1 presents a comparison of previous electrochemical sensors for the detection of AZP.

3.10. Real sample analysis

3.10.1. Real sample preparation

To further evaluate the practical applicability of the developed O-Nd_2WO_6/f-CNF modified electrode for AZP detection, real-sample recovery experiments were conducted using hospital wastewater, river water, and tap water as representative environmental matrices. These matrices were selected to simulate realistic conditions where various inorganic ions, organic residues, and fluctuating pH values may potentially influence electrochemical sensing performance. The corresponding differential pulse voltammetry (DPV) responses obtained for the real samples are presented in Fig. 8**A–C.** Hospital wastewater samples were collected from a local medical discharge outlet, while river water and tap water samples were obtained from nearby environmental and laboratory water sources. Prior to analysis, all samples were filtered through 0.22 μm syringe filters to remove suspended particulates and insoluble impurities. The filtered samples were then used directly without further chemical modification to maintain their natural composition and evaluate the sensor performance under realistic environmental conditions.

3.10.2. Real sample evaluation

For recovery evaluation, known amounts of AZP were spiked into each real sample at three different levels (10 μL, 20 μL, and 30 μL), while the corresponding un-spiked samples served as control measurements. As shown in Fig. 8**A–C**, the un-spiked samples exhibit negligible background electrochemical signals, indicating that the natural matrices do not contain electroactive species that significantly interfere with the AZP detection potential window. After the addition of AZP, well-defined cathodic peaks appear around the characteristic reduction potential, and the peak current gradually increases with increasing spike concentration.

In the hospital wastewater sample Fig. 8**A,** a clear increase in reduction current is observed as the AZP concentration increases, demonstrating that the sensor maintains reliable performance even in highly complex wastewater environments containing organic residues and pharmaceutical contaminants. Similarly, the river water sample Fig. 8**B** shows consistent current enhancement upon AZP addition, indicating that common dissolved ions and natural organic matter present in environmental waters do not significantly hinder the electrochemical response. The tap water sample Fig. 8**C** also displays stable and progressive peak current increases, confirming the sensor capability for AZP detection in drinking-water matrices. The reliable electrochemical responses observed in all three matrices demonstrate the strong anti-interference capability and matrix tolerance of the O-Nd_2WO_6/f-CNF sensing interface. The excellent sensing performance can be attributed to the synergistic interaction between plasma-activated Nd_2WO_6 nanoparticles and the conductive f-CNF framework. Plasma treatment introduces oxygen-rich functional groups and defect sites on the Nd_2WO_6 surface, which enhance the adsorption of AZP molecules through hydrogen bonding and electrostatic interactions. Meanwhile, the highly conductive CNF network provides rapid electron transport pathways, enabling efficient charge transfer even in complex aqueous environments.

The recovery results for hospital wastewater, river water, and tap water samples are summarized in Table S1. The obtained recoveries were in the range of 96.8–102.4% with relative standard deviation (RSD) values below 2.7%, indicating good accuracy and precision of the developed sensor. The consistent responses observed in different environmental samples confirm the reliable analytical performance of the O-Nd_2WO_6/f-CNF modified electrode for AZP detection. These results demonstrate that the proposed sensing platform possesses good stability and selectivity in complex sample matrices. Consequently, the proposed electrochemical platform shows strong potential for practical monitoring of pharmaceutical residues and emerging drug contaminants in environmental water systems

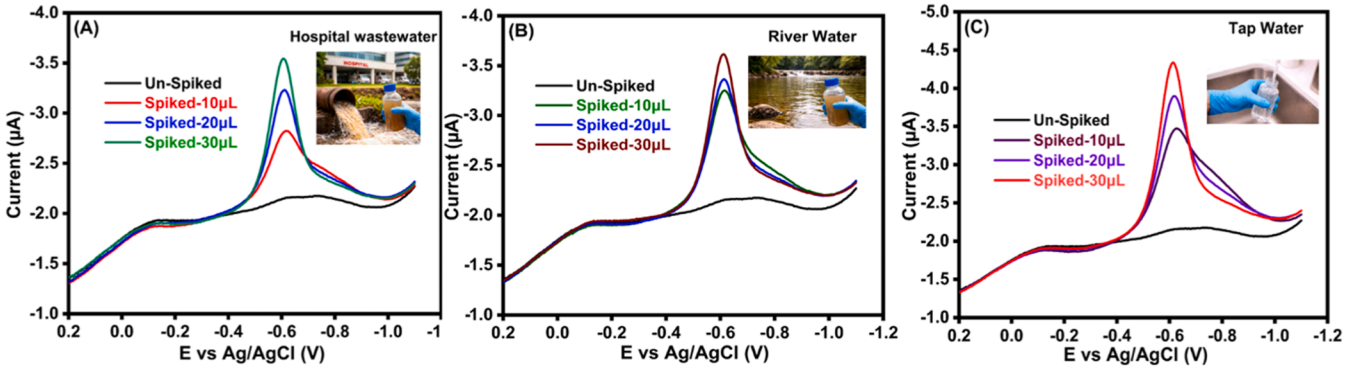

Fig. 8. Real sample analysis of AZP using the O-Nd_2WO_6/f-CNF modified electrode. DPV responses for (A) hospital wastewater, (B) river water, and (C) tap water under unspiked and spiked conditions (10–30 μL). The increased peak current with spiking confirms the reliable detection and good analytical performance of the sensor in real environmental samples.

4. Conclusion

In this work, a defect-engineered O-Nd_2WO_6/f-CNF nanocomposite was successfully developed through a combined hydrothermal, plasma modification, and ultrasonication-assisted approach for the electrochemical detection of AZP. XRD analysis confirmed the formation of crystalline Nd_2WO_6 without impurity phases, while XPS results revealed stable oxidation states and the introduction of oxygen-related active sites after plasma treatment. FESEM and TEM analyses demonstrated the successful anchoring of O-Nd_2WO_6 nanoparticles onto the interconnected CNF network, forming a well-integrated hybrid structure with enhanced surface area and active sites. Electrochemical studies showed that the O-Nd_2WO_6/f-CNF modified electrode exhibited significantly enhanced sensing performance, with a low detection limit of 0.066 μM, high sensitivity of 0.74 μA μM^{-1} cm^{-2}, and a wide linear detection range of (1 μM to 360 μM and 410 μM to 1420 μM). Furthermore, the sensor demonstrated excellent stability, selectivity, and reliable performance in real water samples with satisfactory recoveries of 96.8–102.4% values. This work provides an effective strategy for designing plasma-engineered rare-earth-based nanocomposites as high-performance electrochemical sensors for environmental monitoring of pharmaceutical contaminants.

CRediT authorship contribution statement

Parthasarathi Manimaran: Writing – review & editing, Writing – original draft, Software, Investigation, Formal analysis, Data curation, Conceptualization. **Kumar Gokulkumar:** Writing – review & editing, Writing – original draft, Methodology, Formal analysis, Conceptualization. **Kun-Mu Lee:** Supervision, Resources, Project administration, Funding acquisition, Formal analysis, Conceptualization. **Shih-Hsuan Chen:** Software. **Neeraja Bose:** Software, Resources. **Shen-Ming Chen:** Validation, Supervision, Resources, Methodology, Funding acquisition, Formal analysis.

Declaration of Competing Interest

The authors declare that they have no known competing financial interests or personal relationships that could have appeared to influence the work reported in this paper.

Acknowledgments

The authors gratefully acknowledge financial support from the National Science and Technology Council (NSTC), Taiwan, under Project No. NSTC 111–2223-E-182–001-MY4, NSTC 114–2113-M-027–008. This research was also supported by the Chang Gung University, Taiwan. Project No (URRPD2R0011).

Declaration of Competing Interest

The authors declare that there are no known financial or personal relationships that could have influenced the work reported in this study.

Appendix A. Supporting information

Supplementary data associated with this article can be found in the online version at doi:10.1016/j.jece.2026.123120.

Data Availability

Data will be made available on request.

References

[1] N. Chande, et al., Azathioprine or 6-mercaptopurine for maintenance of remission in Crohn's disease, Cochrane Database Syst. Rev. 1996 (5) (2016).
[2] J.P. Gisbert, Y. González-Lama, J. Maté, Thiopurine-induced liver injury in patients with inflammatory bowel disease: a systematic review, Off. J. Am. Coll. Gastroenterol. | ACG 102 (7) (2007) 1518–1527.
[3] S. Sahasranaman, D. Howard, S. Roy, Clinical pharmacology and pharmacogenetics of thiopurines, Eur. J. Clin. Pharmacol. 64 (8) (2008) 753–767.
[4] S. Meggitt, et al., British Association of Dermatologists' guidelines for the safe and effective prescribing of azathioprine 2011, Br. J. Dermatol. 165 (4) (2011) 711–734.
[5] L. Lennard, TPMT in the treatment of Crohn's disease with azathioprine, Gut 51 (2) (2002) 143–146.
[6] W. Connell, et al., Bone marrow toxicity caused by azathioprine in inflammatory bowel disease: 27 years of experience, Gut 34 (8) (1993) 1081–1085.
[7] S. Siramolpiwat, D. Sakonlaya, Clinical and histologic features of Azathioprine-induced hepatotoxicity, Scand. J. Gastroenterol. 52 (8) (2017) 876–880.
[8] A. Anstey, et al., Pancytopenia related to azathioprine—an enzyme deficiency caused by a common genetic polymorphism: a review, J. R. Soc. Med. 85 (12) (1992) 752–756.
[9] S. Knowles, et al., Azathioprine hypersensitivity-like reations–a case report and a review of the literature, Clin. Exp. Dermatol. 20 (4) (1995) 353–356.
[10] F. Bashal, Hematological disorders in patients with systemic lupus erythematosus, Open Rheumatol. J. 7 (2013) 87.
[11] C. Geiger, et al., Azathioprine-induced suicidal erythrocyte death, Inflamm. Bowel Dis. 14 (8) (2008) 1027–1032.
[12] L. Ferrando-Climent, S. Rodriguez-Mozaz, D. Barceló, Incidence of anticancer drugs in an aquatic urban system: from hospital effluents through urban wastewater to natural environment, Environ. Pollut. 193 (2014) 216–223.
[13] Y. Zhang, et al., Kinetic and mechanistic investigation of azathioprine degradation in water by UV, UV/H2O2 and UV/persulfate, Chem. Eng. J. 302 (2016) 526–534.
[14] M. Jeebhay, S. Mbuli, R. Uebel, Assessment of exposure to chloramphenicol and azathioprine among workers in a South African pharmaceutical plant, Int. Arch. Occup. Environ. Health 65 (1) (1993) S119–S122.
[15] J. Singh, A. Mehta, Rapid and sensitive detection of mycotoxins by advanced and emerging analytical methods: a review, Food Sci. & Nutr. 8 (5) (2020) 2183–2204.
[16] A.H. Ali, High-performance liquid chromatography (HPLC): a review, Ann. Adv. Chem. 6 (1) (2022) 010–020.
[17] Z. Lin, L. He, Recent advance in SERS techniques for food safety and quality analysis: A brief review, Curr. Opin. Food Sci. 28 (2019) 82–87.
[18] K. Gokulkumar, et al., Nanoparticles of SnS on carbon nanofibers for electrochemical detection of vanillin, ACS Appl. Nano Mater. 7 (11) (2024) 13183–13193.
[19] K. Gokulkumar, et al., Sustainable surfactant-free synthesis of MnMoO4/CArbon Nanofiber Composite for Highly Sensitive Detection of Nimesulide in Biological and Pharmaceutical Matrices, ACS Appl. Bio Mater. 8 (10) (2025) 8864–8879.
[20] P. Manimaran, et al., Ni-metal–organic framework/β-cyclodextrin/functionalized carbon black nanomaterials for enhanced electrochemical sensing of metronidazole in environmental and clinical samples, ACS Appl. Nano Mater. 8 (48) (2025) 23260–23272.
[21] K. Gokulkumar, I.J.D. Priscillal, S.-F. Wang, Deep eutectic solvent-mediated synthesis of PDA coated f-CNF doped ZnS nanoparticles for electrode modification: Innovative sensing platform for determination of pollutant 3-nitrophenol, J. Alloy. Compd. 924 (2022) 166561.
[22] S.-J. Huang, et al., Nanoarchitectonics of europium vanadate nanoparticles decorated carbon nanofibers for electrochemical detection of fungicide in fruits, J. Taiwan Inst. Chem. Eng. 161 (2024) 105563.
[23] P. Varatharajan, et al., A wide linear range and highly sensitive electrochemical reduction of environmental hazard (p-Nitrotoluene) using carbon-based hybrid composite (Ti3C2TX@ MnCo2O4), J. Environ. Chem. Eng. 12 (6) (2024) 114301.
[24] E. Baldin, et al., Phase Formation, Polymorphism, Optical Properties, and Conductivity of Nd2WO6-Based Compounds and Solid Solutions, Russ. J. Phys. Chem. A 98 (11) (2024) 2544–2554.
[25] M. Arunpandian, et al., Development of novel Nd2WO6/ZnO incorporated on GO nanocomposite for the photocatalytic degradation of organic pollutants and biological studies, J. Mater. Sci. Mater. Electron. 30 (20) (2019) 18557–18574.
[26] G. Wu, Oxygen plasma treatment of high performance fibers for composites, Mater. Chem. Phys. 85 (1) (2004) 81–87.
[27] M.C. Kim, et al., Surface treatment of metals using an atmospheric pressure plasma jet and their surface characteristics, Surf. Coat. Technol. 174 (2003) 839–844.
[28] D.H. Kim, et al., Uniform area treatment for surface modification by simple atmospheric pressure plasma treatment technique, IEEE Access 7 (2019) 103727–103737.
[29] P. Varatharajan, et al., Ultrasonic synthesis of MOF-based hybrid composite for electrochemical detection of furazolidone antibiotic in food and biological samples, Surf. Interfaces 55 (2024) 105384.
[30] K.L. Klein, et al., Surface characterization and functionalization of carbon nanofibers, J. Appl. Phys. 103 (6) (2008).
[31] D. Senthilkumar, et al., Nanoparticles of neodymium tungstate on reduced graphene oxide for highly sensitive electrochemical detection of Morin in food, ACS Appl. Nano Mater. 8 (37) (2025) 18136–18146.
[32] K. Gokulkumar, et al., Zinc molybdate/functionalized carbon nanofiber composites modified electrodes for high-performance amperometric detection of hazardous drug Sulfadiazine, OpenNano 10 (2023) 100131.

[33] S.C. Vasconcelos, et al., An improved drop casting electrochemical strategy for furosemide quantification in natural waters exploiting chemically reduced graphene oxide on glassy carbon electrodes, Anal. Bioanal. Chem. 412 (26) (2020) 7123–7130.
[34] Y. Bespalko, et al., Structural and transport properties of neodymium tungstates prepared via mechanochemical activation, Ceram. Int. 45 (7) (2019) 9529–9536.
[35] B.M. Abu-Zied, A. Khan, Microwave-assisted synthesis of micro/nano NdO powders, J. Mater. Res. Technol. 9 (5) (2020) 10478–10490.
[36] L. Chao, et al., Tunable transparency and NIR-shielding properties of nanocrystalline sodium tungsten bronzes, Nanomaterials 11 (3) (2021) 731.
[37] S. Jain, et al., Significance of interface barrier at electrode of hematite hydroelectric cell for generating ecopower by water splitting, Int. J. Energy Res. 43 (9) (2019) 4743–4755.
[38] N. Dwivedi, et al., Understanding the role of nitrogen in plasma-assisted surface modification of magnetic recording media with and without ultrathin carbon overcoats, Sci. Rep. 5 (1) (2015) 7772.
[39] B. Akila, et al., Electrochemical detection of carcinogenic roxarsone using CuWO4 nanoparticles, Process Saf. Environ. Prot. (2025) 108299.
[40] P. Manimaran, et al., Development of an ultrasensitive sensor for detecting metol in environmental water samples using ruddlesden-popper type layered perovskite (La2NiO4) combined with graphene oxide, Water Res. 273 (2025) 122998.
[41] J. Anupriya, et al., Enhanced electrochemical performance of in-situ synthesized Cu nanoparticle/C spheres composite for highly sensitive sensing of azathioprine immunosuppressive drug, Composites Part B Engineering 242 (2022) 110079.
[42] C.L. Montgomery, et al., Kinetic analysis of proton-coupled electron transfer at an electrode-immobilized complex, ACS Electrochem. 1 (3) (2024) 303–314.
[43] T. Mutić, et al., Design of NdOCl/Nd2O3 nanocomposite for sensitive and selective electrochemical detection of pesticide Carbofuran in environmental and food samples: Explanation of the sensing mechanism, Electrochim. Acta (2026) 148257.
[44] A. Jeyaraman, et al., Synergistic performance of FeWO4-WO3 composite for enhanced electrocatalytic detection of azathioprine in biological and environmental samples, J. Environ. Chem. Eng. 13 (5) (2025) 117442.
[45] K. Alagumalai, et al., AgBiS2 embedded activated graphene nanolayer for sensing azathioprine in biospecimens, Colloids Surf. A Physicochem. Eng. Asp. 685 (2024) 133243.
[46] R. Pandiyan, P. Rameshkumar, S.-M. Chen, Hydrothermal synthesis of pure phase doughnut-like NiNb2O6 nanostructures decorated reduced graphene oxide for sensitive electrochemical detection of azathioprine in water samples, Process Saf. Environ. Prot. 201 (2025) 107446.
[47] S.P. Sivaji, et al., Promote the electrocatalytic activity through the assembly of hexagonal SnS2/C sphere nanocomposite for determination of the immunosuppressant drug azathioprine in biological samples, Colloids Surf. A Physicochem. Eng. Asp. 667 (2023) 131335.
[48] B. Mutharani, et al., Devising a universal tailored monomer molecular strategy for SiOx/carbon hollow spheres as a synergistic electrocatalyst in azathioprine sensing, Mater. Today Chem. 26 (2022) 101058.
[49] B. Mutharani, et al., Rational assembly of polymer–metal coordination hierarchical superstructures for azathioprine-responsive electrodes in biological samples, ACS Appl. Nano Mater. 5 (11) (2022) 16207–16219.
[50] T.P.G. Balasubramaniyan, et al., Facile fabrication of a Gd2WO6/MWCNT and comparison with halloysite nanotubes for nanomolar quantification of azathioprine in biological and environmental matrices, Chem. Eng. J. (2025) 170506.
[51] F. Goudarzy, J. Zolgharnein, Highly sensitive and selective fluorescence Nano-sensor for azathioprine determination using g-C3N4@ Fe3O4@ CoWO4 nanocomposite; box–Behnken design optimization, Spectrochim. Acta Part A Mol. Biomol. Spectrosc. (2025) 127079.